2026 IEEE International Conference on Robotics and Automation (ICRA 2026)
June 1-5, 2026. Vienna, Austria

Automated Nerve Suturing Using Dual Arm Nanorobotic System Considering Needle Insertion Depth

Chao Qin, Yujie Jiang, Xiang Fu, Chengxi Zhong, and Song Liu*, *Member, IEEE*

***Abstract*— Peripheral nerve injuries represent a significant clinical challenge in reconstructive surgery, traumatology, and neurosurgery, often leading to permanent sensorimotor deficits and diminished life quality. Thus, achieving precise epineurial suturing without nerve fascicle damage and tension remains a long-term aspiration for nerve repair. Yet, current techniques, mostly using direct suturing by surgeons, showcase unavoidable tension and limited functional outcomes. To address them, this work proposes a dual arm nanorobotic system-based approach for highly automated, precise, repeatable nerve suturing. An optimized path planning algorithm is designed leveraging the epineurial thickness estimation in order to control needle insertion depth and suturing trajectory. Due to the natural advantages of nanorobotics and microscope, the developed system can suture nerve with micron-scale diameter within confined space. *Ex-vivo* experiments on three types of rabbit sciatic nerves demonstrated the effectiveness and motion accuracy of 48 microns and 39 microns for two arms. *In-vivo* experiments with anatomic and functional analyses further validated the functional recovery, showing the potential for clinical translation.**

I. Introduction

Peripheral nerves are the primary communication conduits in animals for mediating rapid bidirectional transmission of electrical signals, which are essential for sensory integration and motor control [1, 2]. Peripheral nerve dysfunction and injuries are gradually common and clinically significant, that often lead to permanent sensorimotor deficits and markedly diminished life quality [3]. While injured nerves possess limited intrinsic regenerative capacity [4, 5], the absence of timely and effective intervention leads to severe clinical challenges [6, 7]. Therefore, effective nerve repair remains critical yet highly demanding [8, 9].

Current clinical nerve repair is mostly operated by skilled surgeons, using strategies including primary nerve repair (direct suturing) [10], nerve grafting [11] and nerve guidance conduits to promote nerve regeneration [12–14]. Among these, primary nerve repair is widely clinically favored [7] due to its merits of preserving native neural continuity, avoiding donor-site morbidity or foreign materials, and holding superior potential for reliable functional recovery [15, 16]. However, the limited sensing capabilities, restricted motion dexterity, and fragile microscale structure of nerves make prolonged, repetitive and precise nerve suturing highly challenging for surgeons. These constraints increase the risk of hindering tension-free suturing and ultimately compromising functional recovery [17]. Thus, automated robotic systems, enabling high-precision operations with consistency, hold promise for advancing nerve suturing.

Extensive efforts have been made to robotic suturing, spanning system frameworks, methodological innovations, and integration with advanced sensing modalities. From the system perspective, Pedram *et al.* developed an autonomous suturing framework on the RAVEN IV 6-DOF cable-driven surgical robot, demonstrating needle trajectory execution with a maximum error of 2.07 mm [18]. Similarly, Feng *et al.* proposed the AIRS platform for autonomous intraoperative keratoplasty, achieving intraoperative accuracy within a 1 mm threshold [19]. Complementary efforts have also introduced hand-held robot-assisted microsurgery systems [20, 21], which provide sufficient stability and precision for robotic suturing. From the methodological perspective, multiple strategies have also been investigated. These include optimization of needle grasp configurations and entry point selection based on robotic manipulability analysis [22], and insertion force minimization via optimal force confinement [23]. To further address safety concerns, novel robotic designs have emerged, such as dual stiffness-tunable positioning arms to reduce risk of excessive stress on fragile neural tissues [24]. In addition, advanced perception methods have been integrated, for instance, GAN-based estimation of needle trajectories hidden within tissue [25], path planning refinements and control strategies for trajectory optimization [26–28], and real-time computer vision algorithms for needle tracking and pose estimation through imaging based visual servoing [18, 26, 29].

Collectively, these advances highlight that robotic suturing systems offer improved accuracy, dexterity, and consistency over manual techniques. Nevertheless, when applied to nerve suturing, unique challenges remain largely unaddressed. **First**, existing automated robotic systems do not consider the needle insertion depth, which is critical for epineurial-only penetration without damaging fascicles. **Second**, nerve suturing needs microscale precision that exceeds the millimeter-level precision of most current automated robotic systems [18–21]. Although some robotic systems achieve higher precision [20, 21], they are non-automated, increasing surgeon workload and fatigue while raising the risk of suturing errors and tissue injury. In clinical settings, even minimal epineurial misalignment can impair function due to fascicular mismatch. **Third**, existing path planning methods often neglect constraint of tension-free suturing, a key determinant of successful functional recovery [19, 26, 28].

This work develops a dual arm nanorobotic system-based approach, integrated with a nerve anatomy-based path planning algorithm to ensure safe needle insertion depth and

*This work was supported in part by the National Natural Science Foundation of China under Grants 62303321. (Corresponding author: Song Liu.)

C. Qin, Y. Jiang, X. Fu, C. Zhong and S. Liu are with the School of Information Science and Technology, ShanghaiTech University, China (Email: liusong@shanghaitech.edu.cn).

controlled suturing paths. With the advantages of nanorobotic manipulation and real-time microscopic imaging, the proposed approach achieves reliable suturing of nerves with micron-scale diameters in surgical environments. The main novelties and contributions are specified as:

1) ***Needle Insertion Depth-Considered Path planning***. A path planning algorithm is introduced with incorporation of insertion depth consideration based on the nerve structural reconstruction, epineurial thickness estimation, and needle dynamics modeling, enabling epineurial-only penetration while avoiding fascicular damage.

2) ***Microscale Precision for Automated Nerve Suturing***. Our proposed vision-guided dual arm nanorobotic system-based approach achieves automated microscale precision nerve suturing beyond the millimeter precision achieved by existing robotic systems.

3) ***In-Vivo Validation and Functional Recovery***. We demonstrate the feasibility of the proposed approach through *in-vivo* experiments on live rabbit sciatic nerve, verifying surgical accuracy, tension-free ability, and functional recovery outcomes.

The rest of this paper is organized as follows: Section II elaborates the overall workflow of nerve suturing and the system-based approach with proposed path planning algorithm. Section III presents experimental results demonstrating the effectiveness of our approach, Section IV concludes this paper.

II. Methodology

A. Nanorobot System Setup

The prototyped dual arm nanorobotic system-based approach for nerve suturing, illustrated in Fig. 1, primarily consists of a dual arm nanorobot for nerve suturing execution, a binocular stereo microscopic vision module for visual feedback, and a host computer for control and information processing. The dual arm nanorobot is equipped with two SmartAct SG-1730 microgrippers mounted on the left and right arms. Each arm provides three translational degrees of freedom (DOFs) via three Attocube ECSx3030 piezoelectric nanopositioners (1 nm resolution with 20 mm travel range), and an additional rotational DOF via an Attocube ECR3030 piezoelectric rotator (1 μ° resolution across full 360° rotation). This configuration enables precise and multi-directional manipulation required by nerve suturing. The stereo microscopic vision module involves two Prosilica GC2450 cameras (2448 × 2048 resolution, 15 frames per second) fitted with Coolens DTCM230-36 telecentric lens to minimize optical distortion. Positioned diagonally above the left and right sides, the cameras maintain both grippers within the field of view and depth of view, ensuring clear visualization of the nerve suturing sequence and mitigating image blur. Finally, the host computer executes the control algorithms and information processing routines that govern the nanorobot's coordinated arm movements. It also handles real-time visual feedback from the stereo vision module,

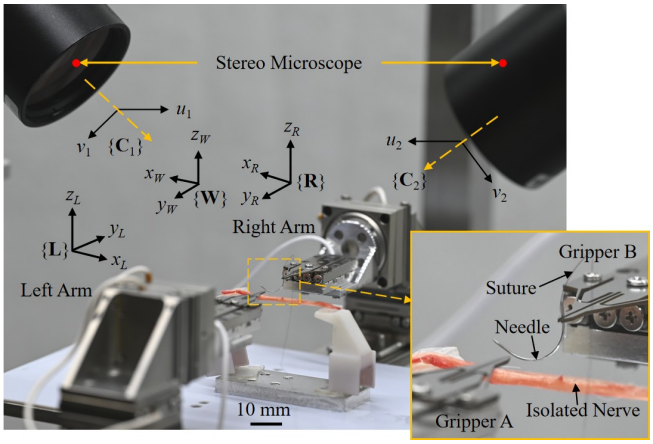

Fig. 1. The dual arm nanorobotic system-based approach for nerve suturing and the coordinate system establishment.

enabling closed-loop control and reliable execution of the nerve suturing process.

For description clarity, two microgrippers mounted on the dual arms are referred to as Gripper A and Gripper B. Then, we established coordinates for nanorobotic system involving camera image coordinates $\{\mathbf{C}_1\}$ and $\{\mathbf{C}_2\}$ for left and right camera, and gripper coordinates $\{\mathbf{L}\}$ and $\{\mathbf{R}\}$ for Gripper A and B. The world coordinates are denoted as $\{\mathbf{W}\}$ within its origin at $\{\mathbf{R}\}$'s initial position. At the starting configuration, XOY planes of $\{\mathbf{L}\}$ and $\{\mathbf{R}\}$ are aligned in parallel.

Specifically, the image Jacobian matrix $\boldsymbol{J_L}$ and $\boldsymbol{J_R}$ of the nanorobotic system are calibrated during the system initialization process, which establishes the hand-eye relationship for the left and right arm relative to the stereo vision setup. Due to the use of telecentric lenses on both cameras, perspective distortion is minimized, ensuring that once calibrated, $\boldsymbol{J_L}$ and $\boldsymbol{J_R}$ remain constant throughout operation. In subsequent procedures such as 3D posture estimation and visual servo control, $\boldsymbol{J_L}$ and $\boldsymbol{J_R}$ are employed to compute the relative position of the target point with respect to each arm by mapping its coordinates from the two 2D images to the corresponding 3D Cartesian space by the pseudo inverse of the image Jacobian matrix. This method not only simplifies the 3D reconstruction process but also improves the accuracy and efficiency of spatial localization by focusing exclusively on the relative position between the target and each nanorobot arm, making it particularly well suited for the automated surgical nerve suturing task. $\boldsymbol{J_L}$ and $\boldsymbol{J_R}$ are calibrated and described with unit in pixel per micrometer as:

$$\boldsymbol{J_L} = \begin{bmatrix} 0.0591 & -0.0025 & 0.0727 \\ 0.0001 & -0.0921 & -0.0023 \\ -0.0567 & 0.0028 & 0.0727 \\ 0.0022 & 0.0923 & -0.0010 \end{bmatrix}, \boldsymbol{J_R} = \begin{bmatrix} -0.0586 & 0.0004 & 0.0727 \\ -0.0028 & 0.0923 & -0.0043 \\ 0.0568 & -0.0012 & 0.0727 \\ -0.0022 & -0.0923 & 0.0010 \end{bmatrix} \quad (1)$$

B. Overview Workflow of Nerve Suturing

The suturing workflow for our dual arm nanorobotic system-based approach is designed to replicate the established principles of microsurgical nerve repair [30, 31], aiming for a tension-free, precise coaptation of nerve ends. The procedure, illustrated in Fig. 2, follows a sequential protocol. The injured nerve ends ($\boldsymbol{E_{N1}}$, $\boldsymbol{E_{N2}}$) are mobilized and

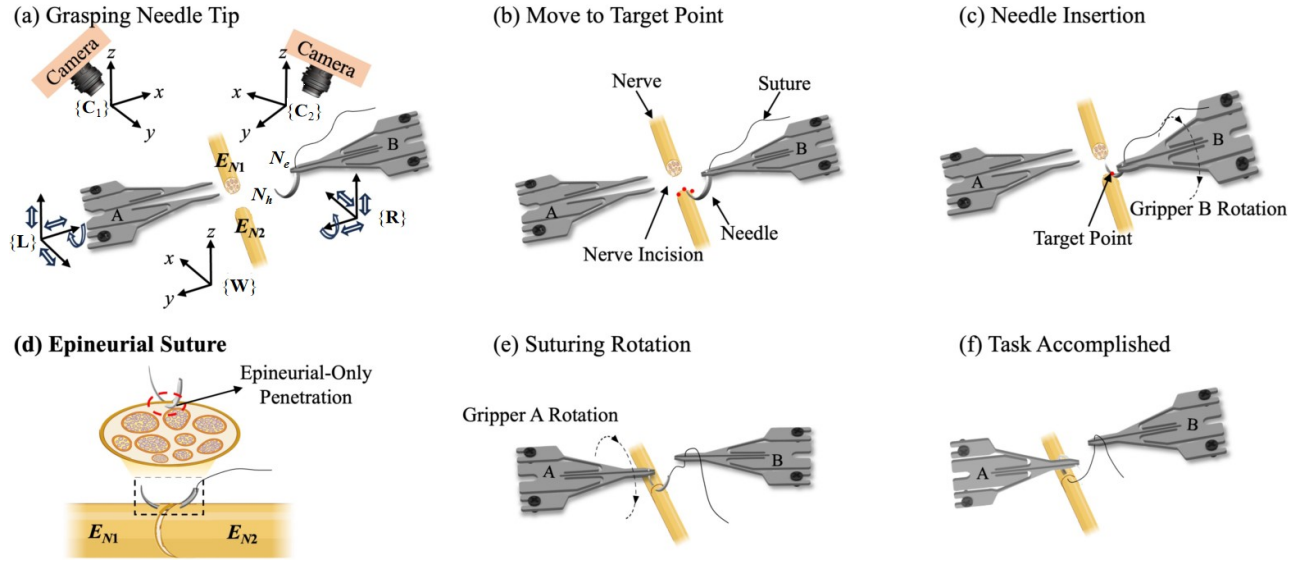

Fig. 2. Schematic pipeline of the automated nerve suturing with coordinated nanorobotic manipulation. (a) Overall system setup. (b) Needle positioning toward the insertion point guided by selected reference points. (c) Needle insertion into the nerve. (d) Suturing rotation process, ensuring epineurial-only penetration while avoiding fascicular damage. (e) Gripper A grasps the needle tip and withdraws it, pulling the suture thread through the nerve tissue. (f) Completion of the suturing task.

aligned with a minimal interfacial gap (Fig. 2(a)). Prior to suturing, the surgeon designates three reference points across this gap via a stereo vision system. The middle reference point is considered as target needle insertion position, and the other two reference points are used to reconstruct a 3D geometric model of nerve cross-section (detailed in Section. II. D). Gripper B, grasping the needle at its suture end (N_e), executes the precomputed trajectory (Fig. 2(b)). The needle is driven through the E_{N2} side, across the gap, and into the E_{N1} side (Fig. 2(c, d)). Visual servo feedback ensures precise tracking of this trajectory. Upon the needle tip (N_h) emerging from E_{N1}, Gripper A grasps it (Fig. 2(e)). Gripper A then completes the trajectory to withdraw the needle, pulling the suture thread through the nerve tissue (Fig. 2(f)). With the suture in place, a knot-tying procedure is performed through coordinated manipulation between Gripper A and Gripper B [32]. Upon completion, the needle is transferred back to Gripper B, and both arms reset to their initial positions, ready for the next suture. This procedure ensures consistent, high-precision suturing under stereo microscopic guidance, adhering to microsurgical principles.

C. Parameterization of Gripper-Needle Configuration

The kinematic relationship between nanorobotic gripper and the curved needle is fundamental for converting a planned needle trajectory into precise arm motions. This section details the configuration when Gripper B holds the needle; the case for Gripper A is identical. As illustrated in Fig. 3, the grasp of a curved needle by the gripper is parameterized by four DOFs. The defined world coordinates {**W**} are given. The rotating coordinates frame of Gripper B is designated as {**R**}. Gripper-world coordinates {**G**} are defined for Gripper B; it coincides with the rotating frame {**R**} at initialization but remains fixed, thus providing a stable reference that simplifies the accounting of Gripper B's rotation about its Y-axis. The needle frame {**N**} is located at the needle head (N_h), with its Z-axis oriented toward the gripper contact point and its Y-axis aligned with the negative tangent direction of the needle curve at N_h.

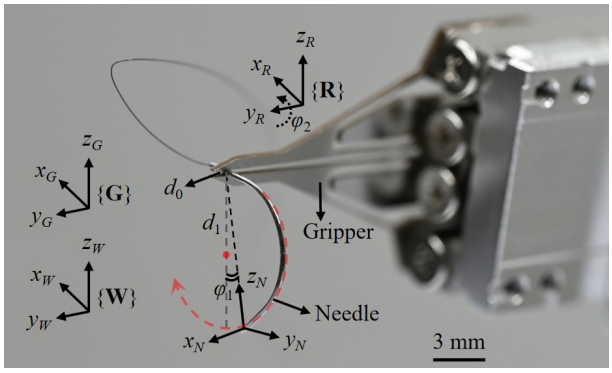

Fig. 3. Illustration for gripper-needle parameterization.

The transformation from the gripper's rotating frame {**R**} to the needle frame {**N**} is mathematically defined by four specific parameters. The needle insertion depth, denoted as d_0, represents the translational distance along the negative Y-axis of {**R**}. The needle radius, a fixed geometric property, is represented by d_1. The tilt angle φ_1 defines the angle between the Z-axis of {**N**} and its vertical projection onto the YOZ plane of {**R**}. The rotation angle φ_2 denotes the counterclockwise rotation of frame {**R**} about its own Y-axis. The complete homogeneous transformation matrix **T** is thus expressed as:

$$
{}^{\mathrm{R}}\mathbf{T}_{\mathrm{N}} = \begin{bmatrix} \mathbf{Ro}(\varphi_1) & \mathbf{P}(\varphi_1, d_1) \\ 0 & 1 \end{bmatrix}
$$
$$
{}^{\mathrm{N}}\mathbf{T}_{\mathrm{R}} = {}^{\mathrm{R}}\mathbf{T}_{\mathrm{N}}^{-1} = \begin{bmatrix} \mathbf{Ro}(\varphi_1)^{\mathrm{T}} & -\mathbf{Ro}(\varphi_1)^{\mathrm{T}}\mathbf{P}(\varphi_1, d_0, d_1) \\ 0 & 1 \end{bmatrix} \tag{2}
$$

where ${}^{\mathrm{R}}\mathbf{T}_{\mathrm{N}}$ and ${}^{\mathrm{N}}\mathbf{T}_{\mathrm{R}}$ are 4×4 matrices, representing position and orientation of {**R**} with respect to {**N**}, and vice versa.

$$
\mathbf{P}(\varphi_1, d_0, d_1) = \begin{bmatrix} -2d_1 \sin\varphi_1 & -d_0 & -2d_1 \cos\varphi_1 \end{bmatrix}^{\mathrm{T}}. \tag{3}
$$

$$\mathbf{Ro}(\varphi_1)=\begin{bmatrix}0 & -\cos\varphi_1 & \sin\varphi_1\\ 1 & 0 & 0\\ 0 & \sin\varphi_1 & \cos\varphi_1\end{bmatrix} \tag{4}$$

Based on the built transformation matrix, the influence of Gripper B's rotation on needle tip motion is analytically determined. To simplify the analysis within the nerve suturing scenario, three key assumptions are introduced from the perspective of frame {**G**}. First, the insertion depth is nullified ($d_0 = 0$), indicating no translational insertion occurs. Second, the tilt angle is zero ($\varphi_1 = 0$), modeling the curved needle as an ideal half-circular arc with its endpoint ***Ne*** grasped by Gripper B. Third, interaction forces between the needle and nerve tissue are neglected, reducing the problem to a purely kinematic formulation. The forward kinematic transformation from frame {**G**} to frame {**R**} is denoted by the 4×4 matrix ${}^{G}\mathbf{T}_{R}$. Then, the transformation matrix ${}^{G}\mathbf{T}_{N}$, describing the influence of Gripper B's rotation on the needle tip position is:

$${}^{G}\mathbf{T}_{N} = {}^{G}\mathbf{T}_{R}\cdot{}^{R}\mathbf{T}_{N}=\begin{bmatrix}0 & -1 & 0 & 0\\ \cos\varphi_2 & 0 & \sin\varphi_2 & 0\\ -\sin\varphi_2 & 0 & \cos\varphi_2 & -2d_1\\ 0 & 0 & 0 & 1\end{bmatrix}. \tag{5}$$

Using the defined transformation matrices and coordinate frames, the discretized kinematics model of gripper-to-needle system is expressed as:

$$\begin{bmatrix}\mathbf{x}^k\\ 1\end{bmatrix}={}^{G}\mathbf{T}_{N}^{-1}(\varphi_0+\Delta\varphi\cdot k)\,{}^{G}\mathbf{T}_{N}(\varphi_0+\Delta\varphi(k-1))\cdot\begin{bmatrix}\mathbf{x}^{k-1}-\sum_{i=0}^{k-1}\boldsymbol{u}_i\\ 1\end{bmatrix}+\begin{bmatrix}\boldsymbol{u}_k+\sum_{i=0}^{k-1}\boldsymbol{u}_i\\ 0\end{bmatrix} \tag{6}$$

where $\mathbf{x}^k$ is a 3×1 vector representing the needle tip position in the world frame {**W**} at timestep k. The term φ_0 denotes the initial rotation angle of the gripper, and $\Delta\varphi$ indicates the rotation increment per timestep. Notably, $\Delta\varphi = 0$ when the nanorobot executes pure translation without rotation. The input $\boldsymbol{u}_k$ is a 3×1 vector corresponding to the translational displacement in {**W**} at timestep k.

D. Nerve Cross-Section's Geometric Modeling

Accurate geometric modeling of the nerve is critical for suturing path planning. The modeling assumes a fresh surgical cross-section, where nerve ends are sharply transected to mimic clinical resection of necrotic tissue. Illustrated as Fig. 4, peripheral nerves typically exhibit elliptical cross-sectional profiles, comprising a central cluster of fascicles surrounded by an outer epineurium [33, 34], which constitutes 30–70% of the cross-sectional area [35, 36]. To avoid fascicular damage [37], suturing must be confined to the epineurium. Accordingly, the nerve cross-section is modeled as a standard ellipse.

The reconstruction process begins with surgeon selecting three reference points (p_M, p_L, p_R) from stereo-microscopic images, defining the minimal gap between nerve ends. Their 3D coordinates in the world frame are computed via Jacobian matrix (Eq. 1 in Sec. II. A). As the cross-section lies primarily in the YOZ plane, the x-coordinates are averaged for planning purposes. The resulting 2D points are denoted $[y_M, z_M]^T$, $[y_L, z_L]^T$, $[y_R, z_R]^T$ for p_M, p_L, p_R, respectively. An ellipse

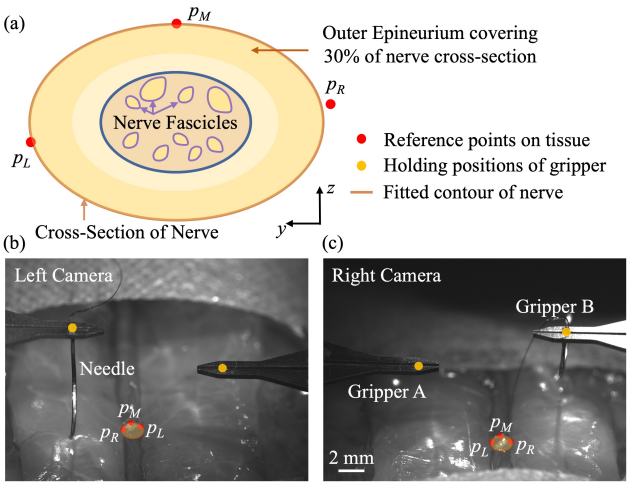

Fig. 4. (a) Schematic illustration of nerve anatomic structure. (b) Illustration of three reference points selected from stereo-microscopic images.

is fitted to these points under the assumption that p_L and p_R represent endpoints of the major axis. The ellipse is described as $(y - h_0)^2 / a_0^2 + (z - k_0)^2 / b_0^2 = 1$, where (h_0, k_0) is the ellipse center, a_0 is the semi-major axis length, and b_0 is the semi-minor axis length:

$$h_0=\frac{y_L+y_R}{2},k_0=\frac{z_L+z_R}{2},a_0=\frac{y_R-y_L}{2},b_0=\left|\frac{z_M-k_0}{\sqrt{1-(y_M-h_0)^2/a_0^2}}\right| \tag{7}$$

The reconstruction is associated with confidence parameter C_p, which is evaluated based on three geometric conditions, including horizontal alignment of p_L and p_R formulated as C_{p1}; ellipse flatness and whether the middle point exhibits the maximum z-coordinate denoted as C_{p2}; and proximity of p_M to the ellipse center is located close to the ellipse center, expressed as C_{p3}. Quantitatively, they are expressed as:

$$C_{p1}=\max(0,1-\frac{|z_L-z_R|}{2K_1b_0})$$

$$C_{p2}=\begin{cases}1, b_0\le a_0\\ \dfrac{K_2(1.2a_0-b_0)}{0.2a_0}, a_0<b_0\le 1.2a_0\\ 0, \text{otherwise}\end{cases}$$

$$C_{p3}=\exp(-(\frac{\tan\varphi_c}{K_3})^2),\tan\varphi_c=|\frac{h_0-y_M}{k_0-z_M}|\in(0,+\infty)$$

Tolerance bandwidths are set to be $K_1 = 0.5$, $K_2 = 0.7$, $K_3 = 2$. Overall confidence $C_p = C_{p1}C_{p2}C_{p3}, C_p \in [0,1]$ must exceed 0.5; otherwise, the points are resampled. This ensures reliable geometric reconstruction for subsequent path planning.

E. Nerve Suturing Path Planning

The motion and posture of grippers are derived from the needle-gripper transformation matrix (Sec. II.C). This section presents path planning to determine an optimal needle insertion path that ensures epineurial penetration without fascicular damage. A fixed center motion (FCM) strategy is adopted, where the needle rotates about its geometric center ***Nc*** [18]. The tissue is assumed homogeneous, and the needle is rigidly clamped without misalignment, moving only along its negative y-axis.

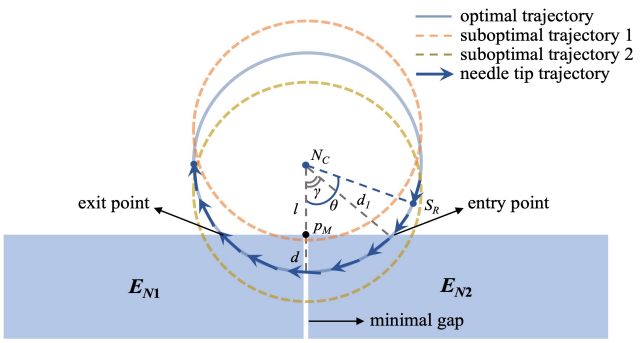

Fig. 5. Optimization of needle path planning.

Relevant FCM parameters are illustrated in Fig. 5. The cross-section in the XOZ plane corresponds to the suturing point p_M (Sec. II.D), where $\boldsymbol{N_c}$ projects onto the nerve surface. The distance between $\boldsymbol{N_c}$ and p_M is denoted l. The rotation start point $\boldsymbol{S_R}$ indicates the initial needle position. The vertical angular displacement θ is defined between the line from $\boldsymbol{S_R}$ to $\boldsymbol{N_c}$ and the vertical axis. The entry angle is γ, and the maximum insertion depth is d. Then, the path planning algorithm is formulated as a constrained optimization:

$$\min_{l,\theta} \mathcal{J}(l,\theta) = \xi^T \boldsymbol{\Phi}(l,\theta) \tag{8.1}$$

$$s.t.\ \ \gamma \le \theta \le \pi - \gamma, \gamma = \arccos\frac{l}{d_1} \tag{8.2}$$

$$\max(0, d_1 - 0.4b_0) < l < d_1 \tag{8.3}$$

where l and θ are the parameters to be optimized. $\boldsymbol{\xi} \in \mathbb{R}^6$ is weight vector for different suturing requirements. Constraint (8.2) prevents collision between needle and nerve surface before insertion, and (8.3) explicitly refuses needle insertion depth with excessive depth. $\boldsymbol{\Phi}(l,\theta) = [\Phi_1, \Phi_2, \Phi_3, \Phi_4, \Phi_5, \Phi_6]^{\mathrm{T}}$ represents the normalized evaluation penalty function matrix for each nerve suturing requirement, detailed as:

$$\boldsymbol{\Phi}(l,\theta) = \begin{bmatrix} \dfrac{1-e^{-a_0 \sin\gamma / b_0}}{1-e^{-a_0/b_0}} \\ 1-\sigma(k_s(\sin\gamma - \min(1, a_0/d_1))) \\ \left(\dfrac{d_1 - l}{0.4b_0}\right)^{\frac{1}{C_{p3}}} \\ \min\left(1, \dfrac{\log(1+l-d_1\cdot\cos\theta)}{\log(1+l)}\right) \\ (1-\sin\theta)^{\frac{1}{C_{p2}}} \\ \mathrm{softplus}\left(\dfrac{l_{\min} + \rho L - l}{m_s L}\right) + \mathrm{softplus}\left(\dfrac{l - (l_{\max} - \rho L)}{m_s L}\right) \end{bmatrix} \tag{9}$$

The penalty function Φ_1 imposes an exponential penalty on the sine of the entry angle γ to minimize tissue deformation forces and control insertion depth, while incorporating the nerve flattening ratio a_0/b_0 to account for its mechanical response. Φ_2 employs a sigmoid function to promote a sufficient span between the needle's entry and exit points, ensuring effective suturing. A soft constraint on insertion depth is introduced in Φ_3, limiting penetration to approximately 40% of the nerve's minor axis and modulating penalty based on reconstruction confidence C_{p3}. Φ_4 applies a logarithmic penalty to minimize non-productive vertical approach distances. To enhance robustness against reconstruction uncertainty, Φ_5 incorporates a safety margin that scales with the confidence parameter C_p. Finally, Φ_6 utilizes softplus functions to discourage optimal solutions near constraint boundaries, thus improving numerical stability and practical feasibility.

The optimization is solved via brute-force search over feasible (l, θ) ranges. The resulting optimal values define the FCM trajectory center $\boldsymbol{N_c}$ and starting point $\boldsymbol{S_R}$. Grippers follow this arc with translation and rotation DOFs.

F. Visual Servo based Needle Control

A closed loop visual servo control scheme (Fig. 6) is integrated into the nanorobotic system-based approach to ensure precise trajectory tracking, allowing real-time motion adjustments and accurate suturing execution. The scheme combines a PI controller with a feedforward term. The feedforward input, defined by the rotation angle θ_k, generates target positions in both stereo microscopic coordinate frame $\boldsymbol{y^F}(k) \in \mathbb{R}^{4\times1}$ and the Cartesian space $\boldsymbol{u_F}(k) \in \mathbb{R}^{3\times1}$ (derived from the kinematic model of the system described in Eq. 6) at each movement step k. Actual grippers positions $\boldsymbol{y}(k) \in \mathbb{R}^{4\times1}$ are obtained from stereo microscopy via template matching [38]. Combining the target position $\boldsymbol{y^F}(k) \in \mathbb{R}^{4\times1}$ provided by feedforward term, the misalignment error $\boldsymbol{y^e}(k)$ in stereo microscopic coordinate frame is calculated and converted to $\boldsymbol{e}(k) \in \mathbb{R}^{3\times1}$ in Cartesian space by the pseudo inverse of image Jacobian matrix J^{-1}, yielding correction term via $\boldsymbol{u_P}(k) = K_P \cdot \boldsymbol{e}(k) + K_I \cdot \sum_{i=0}^{k} \boldsymbol{e}(k) \in \mathbb{R}^{3\times1}$. Then, grippers move with the sum of $\boldsymbol{u_F}(k)$ and $\boldsymbol{u_P}(k)$. The $\boldsymbol{u_P}(k)$ mitigates steady-state error caused by disturbances and stereo vision misalignment during gripper motion, while the $\boldsymbol{u_F}(k)$ improves robustness of gripper trajectory tracking.

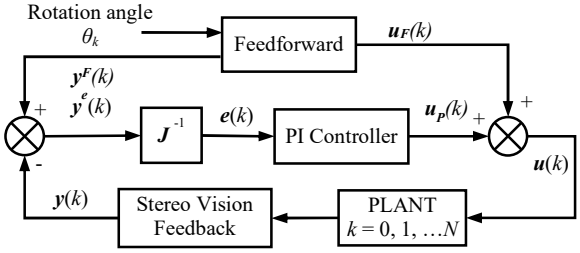

Fig. 6. Control block diagram for visual servo control during nerve suturing.

III. Experiment and Results

To evaluate the effectiveness of the dual arm nanorobotic system-based approach for automated nerve suturing with epineurial-only penetration while avoiding fascicular damage, experimental validation was conducted across two modalities. *Ex-vivo* experiments utilized a 2.0 mm diameter and 6 kPa stiffness isolated rabbit sciatic nerve and a 30 mm long #8-0 micro-suture to simulate microsurgical nerve suturing tasks. Then, *in-vivo* suturing was performed on three types of nerves including living rabbit's sciatic nerve (SN, stiffness of 6 kPa), tibial nerve (TN, stiffness of 5 kPa), and common peroneal nerve (CPN, stiffness of 2 kPa) to assess clinical feasibility. Postoperative anatomic and functional assessments ultimately confirmed nerve functional recovery,

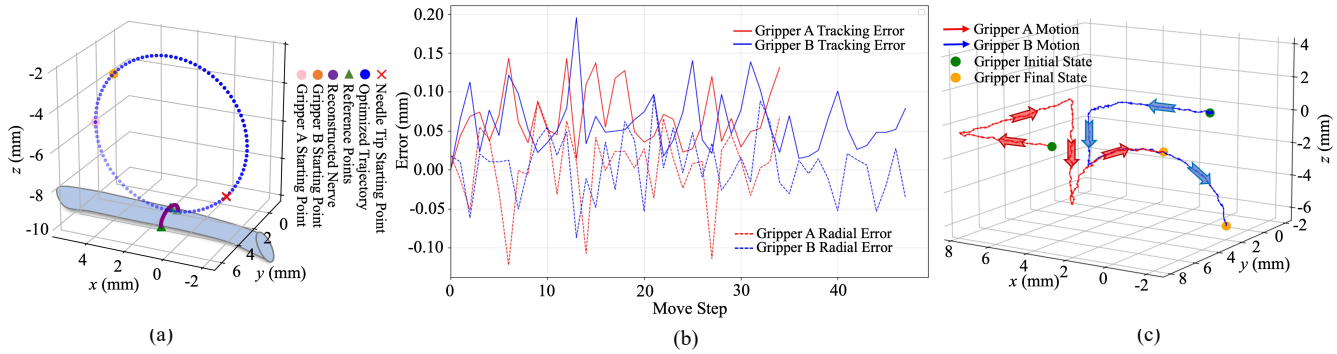

Fig. 7. Experimental results in one suturing process. (a) optimized suturing trajectory and reconstructed nerve surface; (b) the experimental misalignment error of both grippers during the suturing rotation process in XOZ plane; and (c) the motion trajectories of both grippers in 3D space during suturing.

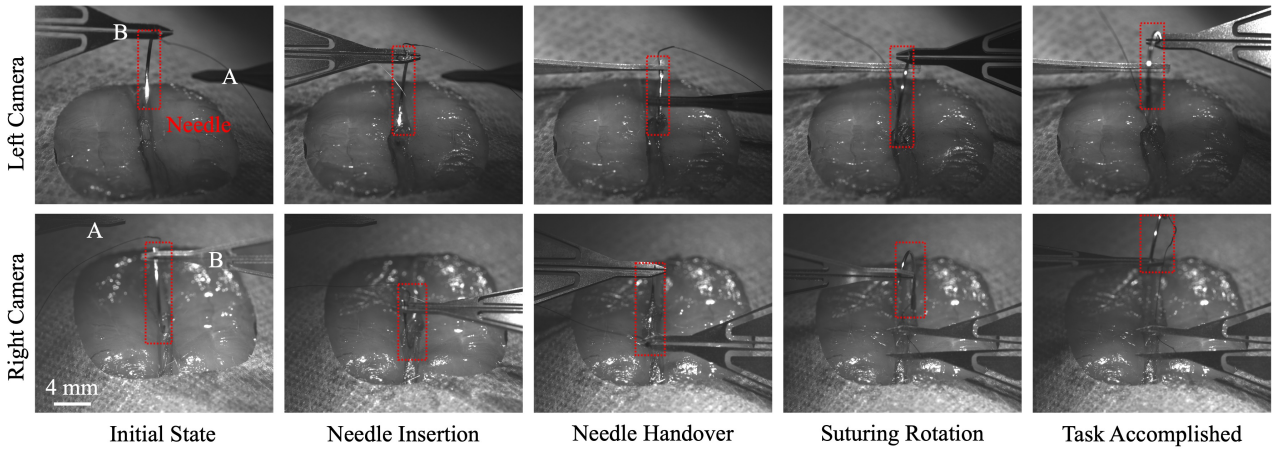

Fig. 8. The sequential images captured from stereo microscope during the *in-vivo* nerve suturing

demonstrating restoration of neural signal transmission across the repaired nerve.

A. Automated Nerve Suturing Demonstration

To evaluate efficacy of the path planning algorithm in controlling needle insertion depth with epineurial-only penetration, and to verify the high precision and robustness of the proposed system-based approach during suturing, an automated nerve suturing experiment is conducted on a 2.0 mm diameter isolated rabbit sciatic nerve using 30 mm long #8-0 micro-suture to validate overall system performance.

Fig. 7(a) illustrates the optimized circular trajectories of both needle and grippers (blue dotted line), together with the reconstructed nerve cross-section (purple line), which are obtained using path planning algorithm (Sec. II.E). Optimized starting points of needle tip (red cross) and grippers (pink and orange dots), and reference points (green triangle) on isolated rabbit sciatic nerve, are also presented. The experiment set optimal weight vector as $\boldsymbol{\xi} = [1.5, 2, 1, 1.5, 2, 1]^{\mathrm{T}}$, slope parameter k_s = 25, bandwidth proportion ρ = 0.15, and declining parameter m_s = 0.03, yielding an optimized insertion depth of 0.19 mm and ensuring epineurial-only penetration. This result indicates that the planned trajectory guarantees a safe insertion depth and a reliable feedforward reference for tracking control.

Fig. 7(b) presents the misalignment errors of the grippers under the purposed visual feedback control during rotation process. The experiments are conducted with rotation angle θ_k = $(3k)°$ and control gains K_P = 0.9, K_I = 0.1. The solid lines denote the absolute misalignment tracking error of each gripper between actual and planned positions on XOZ plane at each move step, with average mean absolute error (MAE) of 67 μm for Gripper A and 61 μm for Gripper B. The dotted lines represent radial errors that quantify the deviation of actual trajectory from the intended target arc, yielding a root mean square error (RMSE) of 48 μm and maximum error of 0.12 mm for Gripper A, and RMSE of 39 μm with 95 μm maximum error for Gripper B. These results demonstrate the effectiveness of visual feedback control in ensuring trajectory consistent with the target, which enhances robustness against disturbances, and improves accuracy for nerve suturing tasks.

Fig. 7(c) presents the complete 3D motion trajectories of both grippers. The blue lines show Gripper B first translating to its starting point and then rotating around the needle center to insert the needle into nerve. Subsequently, the red lines indicate Gripper A translating to its starting point to grasp the needle and rotating along the planned trajectory. These results confirm that the grippers can drive the needle along a precise and well-controlled trajectory.

Fig. 8 presents stepwise images captured by the stereo microscope at different stages on rabbit sciatic nerve. From initial state, Gripper B first inserts the needle into the nerve, followed by Gripper A handling over the needle tip. Subsequently, Gripper A rotates to drive the needle out and complete the suturing. These sequential images demonstrate the successful accomplishment of *in-vivo* nerve suturing.

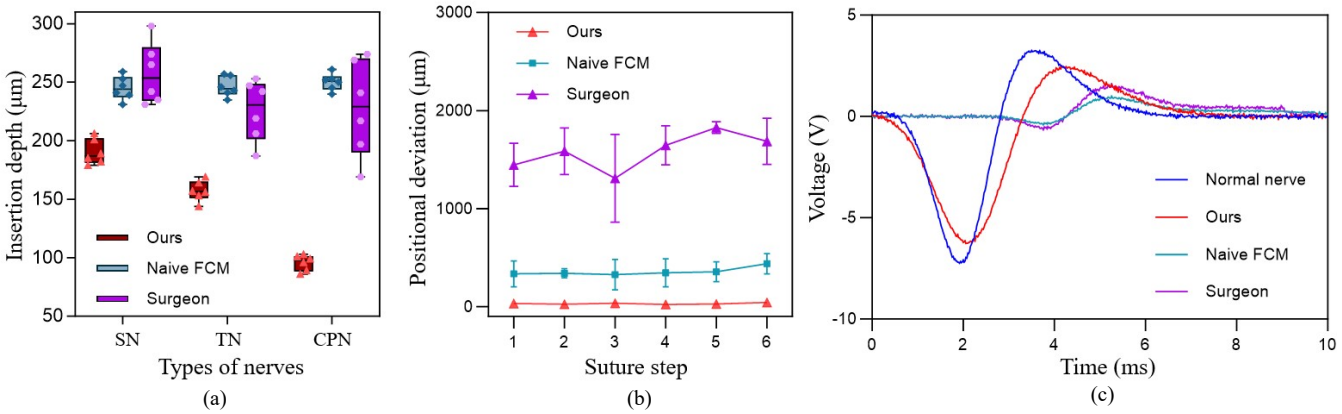

Fig. 9. Comparison results. (a) The insertion depth sutured by our system, naive FCM and surgeon on sciatic nerve (SN), tibial nerve (TN) as well as common peroneal nerve (CPN). (b). The positional deviation during the suturing process with our system, naive FCM and surgeon on sciatic nerve. (c). The electrophysiological signals of normal sciatic nerve and sutured by our system, naive FCM and surgeon.

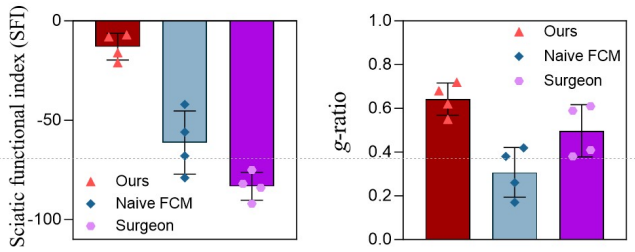

Fig. 10. Comparison experiments of the postoperative validation of nerve suturing performed on our nanorobot and surgeon. (a) The quantification of sciatic function index ($n = 5$) of rabbit. (b). The axon diameter and myelin sheath thickness, shown by the *g*-ratio.

B. Needle Insertion Depth and Postoperative Validation

To evaluate the advantage of the proposed method for needle insertion depth control, we use the developed system to perform interrupted nerve suture on rabbit sciatic nerve (SN), tibial nerve (TN), and common peroneal nerve (CPN)). Insertion depth, positional deviation, physiological electrical signal achieved by our approach were compared with those achieved by a professional surgeon and a naive FCM approach using #8-0 suture, shown as Fig. 9.

As shown in Fig. 9(a), the surgeon group exhibited highly variable insertion depths (average variance: 852), particularly in the thinner CPN, posing a risk of fascicular damage. The naive FCM method demonstrated improved stability but produced insertion depths misaligned with nerve diameters. By contrast, our system-based approach achieved adaptive and stable insertion depths of 190 μm, 157 μm, and 95 μm for SN, TN, and CPN, respectively, with a markedly lower variance of 66. In addition, quantification of nerve traction on isolated rabbit nerves (Fig. 9(b)) confirmed effective tension control throughout suturing. In vivo experiments on rabbit sciatic nerves further verified functional integrity: electrophysiological recordings (Fig. 9(c)) revealed more physiologically relevant signals in nerves repaired with our system compared to the other groups.

The nerve functional recovery after nerve suturing remains a critical benchmark for nerve repair. To assess this, sciatic functional index (SFI) analysis [39] was performed one month post-surgery (Fig. 10(a)). Rabbits treated with our system exhibited superior motor recovery, with restored leg muscle function [39], whereas the other groups showed persistent impairments. Morphological evaluation (Fig. 10(b)) further supported these findings, showing an appropriate axon-to-myelin ratio (average g-ratio: 0.64, within the physiological range of 0.6–0.7) in our system group, while the control groups demonstrated significant mismatches in axon–myelin organization. Together, these results confirm that the proposed system not only enhances surgical accuracy but also promotes functional nerve recovering.

IV. Conclusion and Discussion

This work presents automated nerve suturing using a dual arm nanorobotic system-based approach under stereo microscopy, supported by an optimized path planning algorithm that incorporates nerve anatomy-based epineurial thickness estimation to control needle insertion depth and suturing trajectory. Quantitative *ex-vivo* and *in-vivo* experiments on 2.0 mm rabbit sciatic nerves verified the effectiveness of the approach, while further anatomic and functional analyses confirmed the nerve functional recovery.

It should be noticed that, although the rabbit sciatic nerve provides a suitable animal model, it is relatively stiffer compared to softer and more flexible peripheral nerves encountered in clinical practice, like superficial branches of the ulnar nerve and sural nerve. Such softness and flexibility introduce additional challenges for needle insertion control, path planning, and execution, as they can lead to nerve deformation and position drifts. Our future endeavors will therefore focus on extending the proposed approach to softer, more compliant nerves through refined biomechanical modeling and customized compensation control strategies. To validate these refinements and ensure safety in such sensitive contexts, subsequent studies will also prioritize comprehensive biomechanical and biological evaluation, detailed histological characterization, and sensory functional assessments, alongside enhanced statistical and system robustness to bridge the gap towards clinical translation.

References

[1] Y. Mei, B. L. Zhou, D. Zhong, X. J. Zheng, Y. T. Deng, L. Yu, and B. C. Jiang, "From sensation to regulation: the diverse functions of peripheral sensory nervous system," *Frontiers in Immunology*, vol. 16, May. 2025, Art. no. 1575917.

[2] L. Szczupak, "Functional contributions of electrical synapses in sensory and motor networks," *Current Opinion in Neurobiology*, vol. 41, pp. 99–105, 2016.

[3] C. Miller, A. L. Peek, D. Power and N. R. Heneghan, "Psychological consequences of traumatic upper limb peripheral nerve injury: a systematic review," *Hand Therapy*, vol. 22, no. 1, pp. 35–45, 2017.

[4] A. Höke, "Mechanisms of Disease: what factors limit the success of peripheral nerve regeneration in humans," *Nature Clinical Practice Neurology*, vol. 2, no. 8, pp. 448–454, 2006.

[5] X. Navarro, M. Vivó, and A. Valero-Cabré, "Neural plasticity after peripheral nerve injury and regeneration," *Progress in Neurobiology*, vol. 82, no. 4, pp. 163–201, 2007.

[6] S. Y. Fu and T. Gordon, "Contributing factors to poor functional recovery after delayed nerve repair: prolonged denervation," *Journal of Neuroscience*, vol. 15, no. 5, pp. 3886–3895, 1995.

[7] D. Grinsell and C. P. Keating, "Peripheral nerve reconstruction after injury: a review of clinical and experimental therapies," *BioMed Research International*, 2014.

[8] S. S. Sunderland, "The anatomy and physiology of nerve injury," *Muscle & Nerve*, vol. 13, no. 9, pp. 771–784, 1990.

[9] A. L. Fisse, A. H. Katsanos, R. Gold, K. Pitarokoili, and C. Krogias, "Cross-sectional area reference values for peripheral nerve ultrasound in adults: a systematic review and meta-analysis—part I: upper extremity nerves," *European Journal of Neurology*, vol. 28, no. 5, pp. 1684–1691, 2021.

[10] E. Diao and T. Vannuyen, "Techniques for primary nerve repair," *Hand Clinics*, vol. 16, no. 1, pp. 53–66, 2000.

[11] H. J. Seddon, "Nerve grafting," *The Journal of Bone & Joint Surgery British Volume*, vol. 45, no. 3, pp. 447–461, 1963.

[12] P. Heiduschka and S. Thanos, "Implantable bioelectronic interfaces for lost nerve functions," *Progress in Neurobiology*, vol. 55, no. 5, pp. 433–461, 1998.

[13] C. A. Kubiak, J. Grochmal, T. A. Kung, P. S. Cederna, R. Midha, and S. W. Kemp, "Stem-cell–based therapies to enhance peripheral nerve regeneration," *Muscle & Nerve*, vol. 61, no. 4, pp. 449–459, 2020.

[14] S. Zacchigna and M. Giacca, "Gene therapy perspectives for nerve repair," *International Review of Neurobiology*, vol. 87, pp. 381–392, 2009.

[15] A. G. Nugent and M. Askari, "Epineurial repair," in *Operative Dictations in Plastic and Reconstructive Surgery*, Cham, Switzerland: Springer International Publishing, 2016, pp. 501–502.

[16] C. D. Humphrey and J. D. Kriet, "Nerve repair and cable grafting for facial paralysis," *Facial Plastic Surgery*, vol. 24, no. 2, pp. 170–176, 2008.

[17] G. Hussain, J. Wang, A. Rasul, H. Anwar, M. Qasim, S. Zafar, N. Aziz, A. Razzaq, R. Hussain, J. L. G. De Aguilar, and T. Sun, "Current status of therapeutic approaches against peripheral nerve injuries: a detailed story from injury to recovery," *International Journal of Biological Sciences*, vol. 16, no. 1, pp. 116–134, 2020.

[18] S. A. Pedram, C. Shin, P. W. Ferguson, J. Ma, E. P. Dutson, and J. Rosen, "Autonomous Suturing Framework and Quantification Using a Cable-Driven Surgical Robot," *IEEE Transactions on Robotics*, vol. 37, no. 2, pp. 404–417, 2021.

[19] X. Feng, X. Zhang, X. Shi and L. Li, "AIRS: Autonomous Intraoperative Robotic Suturing Based on Surgeon-Like Operation and Path Quantification in Keratoplasty," *IEEE Transactions on Industrial Electronics*, vol. 71, no. 9, pp. 11115–11124, 2024.

[20] R. A. MacLachlan, B. C. Becker, J. C. Tabares, G. W. Podnar, L. A. Lobes and C. N. Riviere, "Micron: An Actively Stabilized Handheld Tool for Microsurgery," *IEEE Transactions on Robotics*, vol. 28, no. 1, pp. 195–212, 2012.

[21] T. J. van Mulken, R. M. Schols, A. M. Scharmga, B. Winkens, R. Cau, F. B. Schoenmakers, S. S. Qiu, R. R. van der Hulst, X. H. A. Keuter, T. M. A. S. Lauwers, A. A. Piatkowski, J. E. Hommes, D. S. Deibel, J. E. M. Budo, J. Scheerhoorn, and M. E. P. Rijkx, "First-in-human robotic supermicrosurgery using a dedicated microsurgical robot for treating breast cancer-related lymphedema: a randomized pilot trial," *Nature Communications*, vol. 11, no. 757, 2020.

[22] T. Liu and M. C. Cavusoglu, "Needle Grasp and Entry Port Selection for Automatic Execution of Suturing Tasks in Robotic Minimally Invasive Surgery," *IEEE Transactions on Automation Science and Engineering,* vol. 13, no. 2, pp. 552–563, 2016.

[23] V. Kamat, V. Ramakrishnan, Y. Mohnot, H. Jalan, J. Isaac, V. Schorp, Y. Avigal, A. Adler, D. M. Fer, and K. Goldberg, "Automating 2D suture placement," in *2023 IEEE 19th International Conference on Automation Science and Engineering (CASE)*, Auckland, New Zealand, 2023.

[24] J. Guo, J. H. Low, X. Liang, J. S. Lee, Y. -R. Wong and R. C. H. Yeow, "A Hybrid Soft Robotic Surgical Gripper System for Delicate Nerve Manipulation in Digital Nerve Repair Surgery," *IEEE/ASME Transactions on Mechatronics*, vol. 24, no. 4, pp. 1440–1451, 2019.

[25] S. Memida and S. Miura, "Visualization of Surgical Needle Tips Hidden Inside Organs Using Generative Adversarial Networks," in *2024 46th Annual International Conference of the IEEE Engineering in Medicine and Biology Society (EMBC)*, Orlando, FL, USA, 2024.

[26] S. Sen, A. Garg, D. V. Gealy, S. McKinley, Y. Jen, and K. Goldberg, "Automating multi-throw multilateral surgical suturing with a mechanical needle guide and sequential convex optimization," in *2016 IEEE International Conference on Robotics and Automation (ICRA)*, Stockholm, Sweden, 2016, pp. 4178–4185.

[27] R. C. Jackson and M. C. Çavuşoğlu, "Needle path planning for autonomous robotic surgical suturing," in *2013 IEEE International Conference on Robotics and Automation (ICRA)*, Karlsruhe, Germany, 2013, pp. 1669–1675.

[28] J. Shah, P. K. S. Nain, P. Johri and L. Sharma, "Dynamic Path Planning of the Robotic Surgical Needle," in *2024 IEEE International Conference on Information Technology, Electronics and Intelligent Communication Systems (ICITEICS)*, Bangalore, India, 2024.

[29] S. Iyer, T. Looi and J. Drake, "A single arm, single camera system for automated suturing," in *2013 IEEE International Conference on Robotics and Automation (ICRA)*, Karlsruhe, Germany, 2013, pp. 239–244.

[30] M. F. Griffin, M. Malahias, S. Hindocha, and S. K. Wasim, "Peripheral nerve injury: principles for repair and regeneration," *The Open Orthopaedics Journal*, vol. 8, pp. 199–203, 2014.

[31] L. B. Dahlin, "Techniques of peripheral nerve repair," *Scandinavian Journal of Surgery*, vol. 97, no. 4, pp. 310–316, 2008.

[32] Y. Jiang, C. Zhong, C. Qin, Z. Sun and S. Liu, "Synchronous Rotation-Based Knot Tying on Mini-Incisions Using Dual-Arm Nanorobot," *IEEE Transactions on Biomedical Engineering*, vol. 72, no. 6, pp. 1920–1930, 2025.

[33] K. Sonawane, H. Dixit, A. Jayaraj, N. Thota, C. Sekar, and N. R. Thota, "Knowing It Before Blocking It: The ABCD of the Peripheral Nerves: Part A (Nerve Anatomy and Physiology)," *Cureus*, vol. 15, no. 7, Jul. 2023, Art. no. e41771.

[34] S. J. Oh, *Color Atlas of Nerve Biopsy Pathology*, 1st ed. London, UK: CRC Press, 2001.

[35] K. Nawrotek, M. Tylman, K. Rudnicka, J. Gatkowska, and M. Wieczorek, "Epineurium-mimicking chitosan conduits for peripheral nervous tissue engineering," *Carbohydrate Polymers*, vol. 152, pp. 119–128, Nov. 2016.

[36] B. Kundalić, S. Ugrenović, I. Jovanović, et al., "Morphometric analysis of connective tissue sheaths of sural nerve in diabetic and nondiabetic patients," *BioMed Research International*, vol. 2014, Jul. 2014, Art. no. 870930.

[37] A. L. Dellon and S. E. Mackinnon, *Surgery of the Peripheral Nerve*. New York, NY, USA: Thieme Med Publishers, 1988.

[38] X. Qi and L. Miao, "A template matching method for multi-scale and rotated images using ring projection vector conversion," in *2018 IEEE 3rd International Conference on Image, Vision and Computing (ICIVC)*, Jun. 2018, pp. 45–49.

[39] L. Kong, X. Gao, X. Yao, H. Xie, Q. Kang, W. Sun, Z. You, Y. Qian, and C. Fan, "Multilevel neurium-mimetic individualized graft via additive manufacturing for efficient tissue repair," *Nature Communications*, vol. 15, no. 6428, 2024.